ACS Photonics

Article

Cite This: ACS Photonics XXXX, XXX, XXX−XXX

pubs.acs.org/journal/apchd5

Compact Cavity-Enhanced Single-Photon Generation with Hexagonal Boron Nitride

Tobias Vogl,*[,†,§] Ruvi Lecamwasam,[†] Ben C. Buchler,[†] Yuerui Lu,[‡] and Ping Koy Lam*[,†]

[†]Centre for Quantum Computation and Communication Technology, Department of Quantum Science, Research School of Physics and Engineering, The Australian National University, Acton, ACT 2601, Australia

[‡]Centre for Quantum Computation and Communication Technology, Research School of Electrical, Energy and Materials Engineering, The Australian National University, Acton, ACT 2601, Australia

Supporting Information

ABSTRACT: Sources of pure and indistinguishable single-photons are critical for near-future optical quantum technologies. Recently, color centers hosted by two-dimensional hexagonal boron nitride (hBN) have emerged as a promising platform for high luminosity room temperature single-photon sources. Despite the brightness of the emitters, the spectrum is rather broad and the single-photon purity is not sufficient for practical quantum information processing. Here, we report integration of such a quantum emitter hosted by hBN into a tunable optical microcavity. A small mode volume of the order of λ^3 allows us to Purcell enhance the fluorescence, with the observed excited state lifetime shortening. The cavity significantly narrows the spectrum and improves the single-photon purity by suppression of off-resonant noise. The complete device, including all optics, driving electronics, and control units, is compact and integrated in a small volume of $10 \times 10 \times 10$ cm^3, allowing for portable usage in mobile applications.

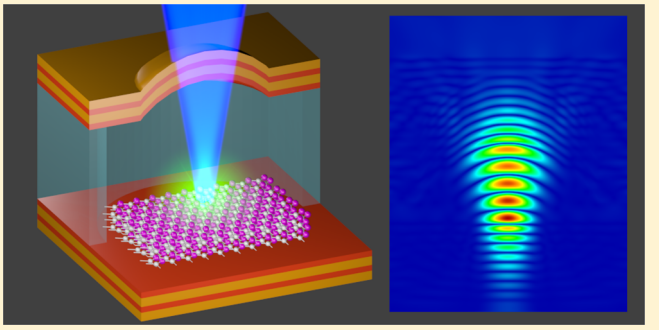

KEYWORDS: *2D materials, fluorescent defect, single-photons, quantum emission, microcavity, Purcell enhancement, quantum information*

Near-future optical quantum information processing[1] relies on sources of pure and indistinguishable single-photons. Promising candidates include quantum dots,[2] trapped ions,[3] color centers in solids,[4] and single-photon sources (SPSs) based on heralded spontaneous parametric down-conversion.[5] The recent discovery of fluorescent defects in two-dimensional (2D) materials has added yet another class of quantum emitters to the solid-state color centers. Stable quantum emitters have been reported in the transition metal dichalcogenides WSe_2,[6−10] WS_2,[11] $MoSe_2$,[12] and MoS_2.[13] The optical transition energies for these emitters, however, are located in close vicinity to the electronic band gap. Thus, cryogenic cooling below 15 K is required to resolve the zero phonon lines (ZPLs). For room temperature quantum emission, defects hosted by large band gap materials are ideal, as has been demonstrated in 2D hexagonal boron nitride (hBN).[14−16] In this case, the energy levels introduced by the defects into the band structure are well isolated. The large band gap of 6 eV[17] also prevents nonradiative decay, which in turn allows for high quantum efficiencies. Unlike solid-state quantum emitters in 3D systems, the 2D crystal lattice of hBN allows for an intrinsically high extraction efficiency. More precisely, the single-photon emitters have an in-plane dipole resulting in out-of-plane emission, where the emitters are not surrounded by high refractive index materials. Hence, total internal or Frensel reflection does not affect the collection of the single-photons. Furthermore, 2D crystals can be easily attached by van der Waals forces to components such as fibers or waveguides, making them suitable for integration with photonic networks.[18,19] The exceptionally high thermal and chemical robustness of hBN benefits the durability of the quantum emitters, achieving long-term stable operation[20] over a huge temperature range,[21] as well as high resistance to ionizing radiation.[22]

In spite of large experimental research efforts and theoretical calculations,[23,24] the exact nature of the defects yet has to be determined. Furthermore, the identification is hampered by the large variations of the lifetime and ZPL wavelength from defect to defect. Lifetimes ranging from 0.3 up to 20 ns[18,20] and ZPLs in the UV[25] and the full visible spectrum[15,26] have been reported. In addition to naturally occurring defects,[14] the emitters can also be created artificially using diverse methods, including chemical etching,[27] plasma etching,[20,28] irradiation with γ-rays,[22] ions,[29] and electrons[29,30] as well as near-deterministic stress-induced activation.[31] Although most researchers agree that quantum emitters in hBN provide a number of unique opportunities, the performance still lags

Received: February 25, 2019
Published: June 26, 2019

DOI: 10.1021/acsphotonics.9b00314
ACS Photonics XXXX, XXX, XXX−XXX

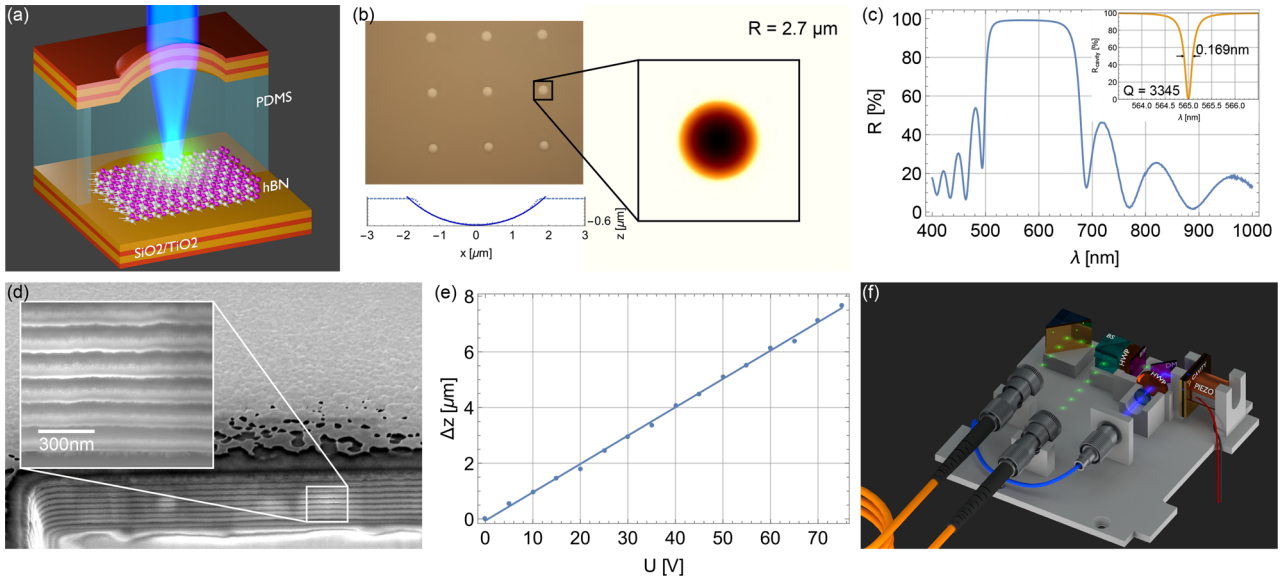

Figure 1. Design and fabrication. (a) The microcavity consists of a hemispherical and flat mirror (only two stacks shown on either sides). The quantum emitter hosted by hBN emits confocally with the excitation laser. A PDMS spacer sets the cavity length. To prevent influence of the polymer on the emitter, the PDMS is etched in the middle. (b) Microscope image of the array of hemispheres (not all 64 shown). The surface profile of the hemisphere actually used for the cavity is shown in the right inset. The bottom inset shows the height profile through an arbitrarily chosen axis. The solid blue line shows an ideal cross section of a hemisphere with radius 2.7 μm. (c) Reflectivity of the coating measured by spectrophotometry, with $R = 99.2\%$ at the target wavelength $\lambda = 565$ nm. The inset shows the calculated cavity reflectivity based on the coating. (d) SEM image (immersion mode) of the mirror stacks, coated with a layer of gold. The sample is tilted by 52°, so the image is skewed in the vertical direction. The lighter areas in the cross section are regions which have been imaged with a magnification of 125 000× (see inset). The intense electron beam makes the surface reactive, and carbon-contaminations by residual organic materials in the SEM chamber are bonded at these areas. (e) Thickness change of a PDMS film with driving voltage reveals linear tuning with 102 nm·V^{-1}. (f) Design of the optics platform (all components to scale). A polarization maintaining fiber (blue) guides the excitation laser from the diode below the platform. The laser is focused to the diffraction limit into the cavity onto the defect. The single-photons transmit through the dichroic mirror (DM) and are additionally band-pass filtered (BPF). Next, they are split by a 50:50 beam splitter (BS) and fiber-coupled into multimode fibers.

behind state-of-the-art SPSs. Moreover, the reported quality of single-photons from hBN is not sufficient for practical quantum information processing like quantum key distribution (QKD)[32] or photonic quantum computing.[33]

A straightforward path for improving the performance of a spontaneous emission process is to use the Purcell effect by coupling the emitter to an optical resonator.[34] The optical resonator reduces the number of modes the emitter can couple to, thereby enhancing emission into the resonant modes. This even works in the "bad-emitter" regime, when the emitter line width is larger than the cavity line width.[35] Work on cavity-integration of emitters in 2D materials has been reported, with quantum emitters hosted by WSe_2 coupled to plasmonic nanocavities[36,37] and microcavities.[38] Quantum emitters hosted by hBN have been coupled to plasmonic nanocavities.[39] Hexagonal boron nitride can also be used to fabricate photonic crystal cavities; however, this makes the required spectral matching between optical cavity mode and emitter difficult.[40] Yet, the performance is still not sufficient for use in quantum information experiments.

In this article, we report room temperature single-photon emission from multilayer hBN flakes coupled with a microcavity. The plano-concave cavity fully suppresses the phonon sideband (PSB) and other off-resonant noise, while at the same time greatly enhances directionality and the spontaneous emission rate. The hemisphere is fabricated using focused ion beam (FIB) milling, allowing for a small radius of the accurate and precise curvature. This leads to an ultrasmall mode volume on the order of λ^3. We fully characterize the SPS and assess its feasibility for quantum key distribution and quantum computing. Moreover, the single-photon source in its current configuration is compact and fully self-contained within 10 × 10 × 10 cm^3, including all optics, driving electronics and control units.

DESIGN AND FABRICATION

The confocal microcavity consists of a hemispherical and a flat mirror, with the hBN flake hosting the quantum emitter transferred to the focal point of the cavity (see Figure 1(a)). The hemisphere spatially confines the cavity mode to the location of the emitter and is fabricated using I_2-enhanced focused ion beam milling.[41,42] We fabricated arrays of 64 hemispheres per substrate with varying geometrical parameters. The surface roughness could be minimized by adding I_2-gas during the milling process. With the FIB we can achieve radii of curvature down to <3 μm (see Figure 1(b)). We initially characterized the hemispheres using an atomic force microscope (AFM) and phase-shift interferometry (PSI). The characteristic parameters extracted with both methods agree well, which allows us to use the much faster PSI for the characterizations. The hemisphere profile shown in Figure 1(b) has a radius of 2.7 μm and root-mean-square deviations <1 nm from an ideal hemisphere (see Supporting Information S1). Note that we did not fabricate full hemispheres and the shapes deviate at the edges (which is due to a conductive coating to prevent charging effects during the milling). Both the flat and concave substrate are coated with 9 pairs of alternating dielectric quarter wave stacks (SiO_2/TiO_2), deposited using plasma sputtering. We measured a reflectivity

DOI: 10.1021/acsphotonics.9b00314
ACS Photonics XXXX, XXX, XXX−XXX

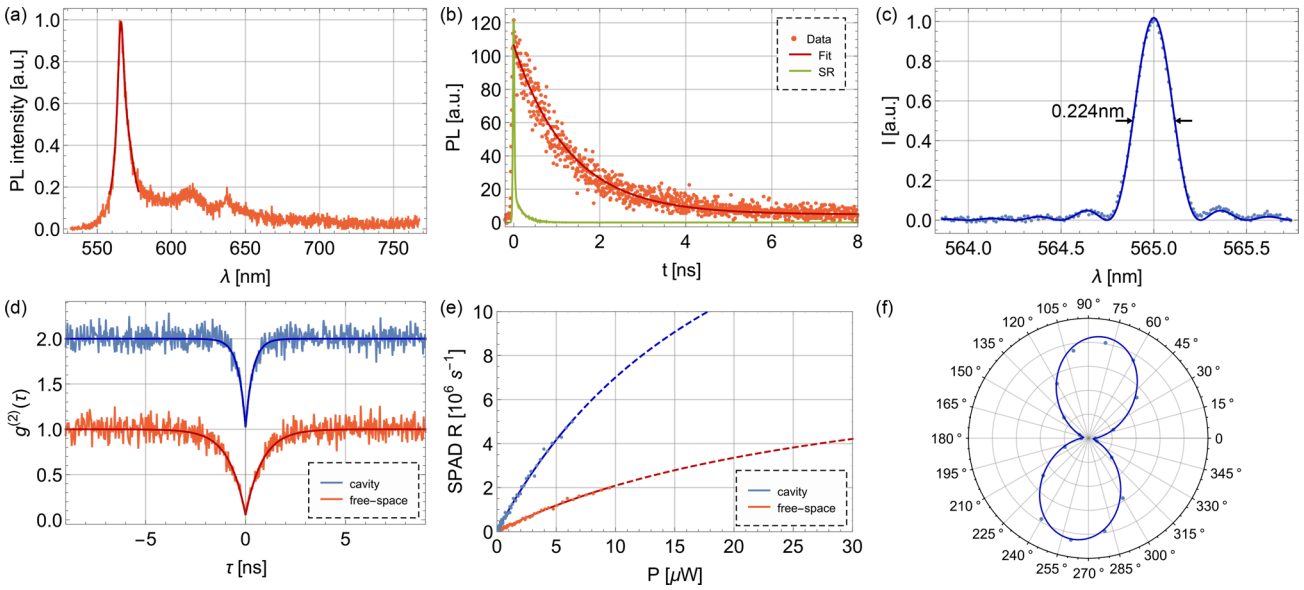

Figure 2. Performance of the single-photon source. (a) Free-space spectrum after off-resonant excitation measured in-reflection and coupled to a grating-based spectrometer. From a Lorentzian fit we extract the ZPL at 565.85(5) nm and a line width (fwhm) of 5.76(34) nm. (b) Time-resolved photoluminescence reveals an excited state lifetime of τ = 897(8) ps. The exponential fit function is convoluted with the system response (SR). (c) The cavity narrows the spectrum down to 0.224 nm (fwhm). The spectrum has been recorded using a high-resolution Fourier-transform spectrometer. The finite scan range results in the spectrum being convoluted with the system response function (of the form of a $\mathrm{sinc}^2(x)$), which in turn leads to the side lobes. (d) When comparing free-space with cavity-coupled emission, the second-order correlation function measurements show a decrease of g_0^2 from 0.051(23) or −12.9 dB to 0.018(36) to −17.4 dB and shortening of the lifetime from 837(30) to 366(19) ps due to the Purcell effect. The cavity data is vertically offset for clarity. (e) The cavity increases the single-photon count rate, even at lower excitation power. This is because of the shortening of the lifetime due to the Purcell effect, but also due to an enhanced collection efficiency with the cavity. (f) The emission is dipole-like, as the projections on different polarization directions show. The solid line is obtained by fitting a $\cos^2(\theta)$ function.

of 99.2% at a wavelength of 565 nm (see Figure 1(c)). The calculated resulting cavity reflectivity (see Figure 1(c), small inset) has a fwhm of 0.169 nm, corresponding to a quality factor of Q = 3345. The stopband of the cavity requires the single-photon excitation laser to be shorter than 504 nm, otherwise the cavity has to be resonant at both the ZPL and excitation wavelength. By cutting through one of the stacks with a FIB and imaging with a scanning electron microscope (SEM) in immersion mode (see Figure 1(d)), we see that stacking defects occur, as expected predominantly in higher layers. This is not an issue, however, as they are still $\ll \lambda$. The reflectivity is most likely limited by incorporated residual nitrogen, leading to scattering losses. It should also be noted that at a high magnification (see inset) the stacks show a spotted pattern. This is actually redeposition of atoms during the milling with the FIB. The backsides of the substrates were coated with antireflective coatings, consisting of a single quarter wave layer MgF_2. This reduces the reflection losses at the glass−air interface from 4.33% to 2.97%.

Multilayer hBN flakes have been placed onto the flat mirror via clean polymer transfer (see Methods). The more common direct dry transfer was not used as this usually also transfers residues. The hBN crystals were treated using an oxygen plasma followed by rapid thermal annealing under an Ar atmosphere.[20] Using plasma etching, defects with their ZPL primarily around 560 nm form, well within the stopband of the coating. Finally, a tunable polymer spacer is deposited onto the concave mirror. A piezoelectric actuator provides the tuning force and compresses the polymer. In contrast to monolithic cavities,[43−45] this approach allows for in situ tuning of the cavity length. The tuning capability is essential, since the exact position of the ZPL cannot yet be controlled and the optical cavity mode has to be artificially matched to the spectrum of the emitter.[40] Due to a suitable Young's modulus and the ability to deform reversibly, we selected PDMS (polydimethylsiloxane) from a range of polymers (see Supporting Information S2). Figure 1(e) shows that the compression of the PDMS film is linear with the driving voltage at the actuator, with a tuning of 102 nm·V^{-1}. This allows us to easily lock the cavity to any arbitrary wavelength. To prevent influence of the PDMS on the emitter, the PDMS was deposited on the opposing mirror and etched around the array prior to contacting with the other mirror.

The cavity mirrors, together with all in- and out-coupling optics, were aligned and glued to a monolithic platform (see Figure 1(f) and Supporting Information S3). Prior to the gluing each component, held with vacuum tweezers, has been aligned with a motorized 6-axis translation stage. This greatly reduces the size of the complete SPS, at the cost of limiting the tunability to only cavity length. Changing the radius of curvature of the cavity as demonstrated in a similar experiment is thus not possible.[38] Nevertheless, the compact size of optics, as well as choice of electronics and excitation laser, allow us to reduce the size of the full experiment to 10 × 10 × 10 cm^3. This reduces the size of the source further compared to previous compact photoluminescence (PL) setups.[46] This also allows for portable usage of the single-photon source in mobile applications.

PERFORMANCE OF THE SINGLE-PHOTON SOURCE

Prior to the cavity experiments we performed a free-space characterization of the quantum emitters on the mirrors. All measurements were carried out at room temperature. The

DOI: 10.1021/acsphotonics.9b00314
ACS Photonics XXXX, XXX, XXX−XXX

defects were located using confocal PL mapping under off-resonant excitation at 522 nm. As hBN itself is optically inactive in the visible spectrum, all emission originates from the defects or surface contaminants. Each crystal is scanned with a resolution of 0.5 μm. For the cavity, we selected a suitable defect with a ZPL at 565.85(5) nm and a Lorentzian line width (fwhm) of 5.76(34) nm (see Figure 2(a)). The PL spectrum shows the typical asymmetric line shape. Note that this is not a result of partial suppression of the long pass filter used to block the pump laser (see Methods), but rather the PSB being adjacent to the ZPL. The defect emits 63.2% into its ZPL. We note that the emission >580 nm originates from surface contaminants activated during the annealing and is usually filtered out (see Methods). Alternatively, annealing in a reactive environment can burn off these contaminants. Time-resolved PL (TRPL) reveals a single-exponential decay with a lifetime of 897(8) ps (see Figure 2(b)). The fit function is convoluted with the system response (also shown in Figure 2(b)) in order to reproduce the observed data.

For the cavity experiments, we used a custom-built high-resolution Fourier-transform spectrometer (FTS), instead of the grating-based spectrometer. After aligning the concave to the flat mirror and coupling the emitter with the cavity mode, we saw an improved spectral purity (see Figure 2(c)), with the single-photon line width narrowing down to 0.224 nm (fwhm), corresponding to a cavity quality factor of 2522. In frequency space the line width corresponds to 210.6 GHz. The spectrum, however, shows side lobes, which do not originate from higher-order transverse cavity modes. The transverse mode spacing is much larger than the difference in observed peak positions (see Supporting Information S4). These peaks are artifacts from the finite scan range of the FTS which results in a truncated Fourier-transform. Convoluting this response (which is of the form of $\mathrm{sinc}^2(x)$) with a Lorentzian reproduces the observed data.

The lifetime cannot be measured directly using time-resolved PL, as the wavelength of the ultrashort pulsed laser is within the stopband of the cavity. For a single-photon emitter, however, it is possible to extract the lifetime directly from the second-order correlation function, which we measure using a Hanbury Brown and Twiss (HBT)-type interferometer. For the emitter in the cavity, we measure $g_0^2 \equiv g^{(2)}(\tau = 0) = 0.018(36)$ (see Figure 2(d)) and from the fit we extract a lifetime of 366(19) ps (see Methods). For a fair comparison of free-space and cavity-enhanced lifetimes we compare the correlation function measurements in free-space and with the cavity. The $g^{(2)}(\tau)$ for the uncoupled emitter dips only to 0.051(23) and has a lifetime of 837(30) ps. The lifetimes measured with time-resolved PL and extracted from the $g^{(2)}(\tau)$ measurements agree reasonably well, even though we note that the 897(8) ps from the TRPL measurement is likely more accurate. While $g_0^2 = 0$ is within the error margin for the cavity-coupled emitter, more accurate measurements are required to reduce the error margin to extract the true value of g_0^2. A small error margin on correlation function measurements can typically be achieved with ultrashort pulsed excitation.[47,48] We also calculated the background correction term[49] and found that it is smaller than the significant digits of our measurement result ($<5 \times 10^{-5}$), so we conclude that any deviation from 0 is not due to detector dark counts, but rather other noise sources excited through the laser. If we directly compare g_0^2 of the uncoupled and cavity-enhanced emitter, however, we see a reduction of a factor of 2.83. Such reduction can typically be achieved in the "bad-emitter" regime and means that off-resonant noise sources are successfully suppressed. A narrower cavity line width could thus further reduce g_0^2. It is worth noting that many applications require the generation of single-photons on-demand, which can be achieved by pulsed excitation of the emitter. As already mentioned, our pulsed laser is within the stopband of the cavity, making it impossible to match excitation and emission wavelength for this laser due to the large free spectral range. The values for the second-order correlation function, however, can be equal for both continuous and pulsed excitation schemes,[50] allowing for simply replacing the continuous excitation laser in our experiment with a suitable pulsed laser for potential quantum information experiments (see below).

The ratio of free-space (or rather half-sided cavity) to cavity-coupled lifetime is $f = 2.29$. The effective Purcell enhancement is given by

$$F_p^{\mathrm{eff}} = \frac{3}{4\pi^2}\lambda^3\frac{Q^{\mathrm{eff}}}{V} \tag{1}$$

with Q^{eff} being the effective quality factor and V being the cavity mode volume. This can be calculated by integrating over the Gaussian fundamental mode in a resonator:

$$V = \int_0^{2\pi}\int_0^{\infty}\int_0^{L'} \mathrm{d}\phi\ \mathrm{d}r\ \mathrm{d}z\ \sin^2\left(\frac{2\pi z}{\lambda}\right) r\ \exp\left(-2r^2/w_0^2\right) = \frac{\pi}{4}L' w_0^2 \tag{2}$$

where L' is the effective cavity length (see below for the calculation) and $w_0^2 = \frac{\lambda}{\pi}\sqrt{L'r - r^2}$ is the cavity waist, determined by the effective cavity length and r, the radius of the hemisphere. We calculate the mode volume to be 1.76 λ^3. In the "bad-emitter" regime the effective quality factor $Q^{\mathrm{eff}} = \frac{\lambda}{\Delta\lambda_{\mathrm{cav}} + \Delta\lambda_{\mathrm{em}}}$ has to be used, which is dominated by the emitter dynamics. It should be mentioned that this is only an approximation and it is more accurate to calculate the overlap integral of the photonic density of states of the cavity and electronic density of states of the emitter. In addition, this effective Purcell factor is different from the ratio f, because the dielectric environment of the mirror is modifying the available density of states, whereas the Purcell factor is the ratio of vacuum (or true free-space) to cavity lifetime. We calculate the effective Purcell factor to be 4.07. This also allows for the direct calculation of the quantum efficiency,[38] given by

$$\eta = \frac{f - 1}{f + F_p^{\mathrm{eff}} - \varepsilon f} \tag{3}$$

where ε is the Purcell factor caused by the mirror and is determined by finite-difference time-domain (FDTD) simulations. For our mirror we find $\varepsilon = 1.68$ (see Supporting Information S5) and thus the quantum efficiency is 51.3%.

The cavity also modifies the power saturation behavior (see Figure 2(e)), with an increased single-photon count rate even at lower excitation power. This is a result of the Purcell enhancement, which makes the emitter brighter, but also from the increased collection efficiency of the cavity, as the emitter predominantly emits into the cavity mode. The low excitation power also assists the single-photon count rate stability, because at low excitation power the emitters show no blinking or photobleaching. This is particularly important as the

DOI: 10.1021/acsphotonics.9b00314
ACS Photonics XXXX, XXX, XXX−XXX

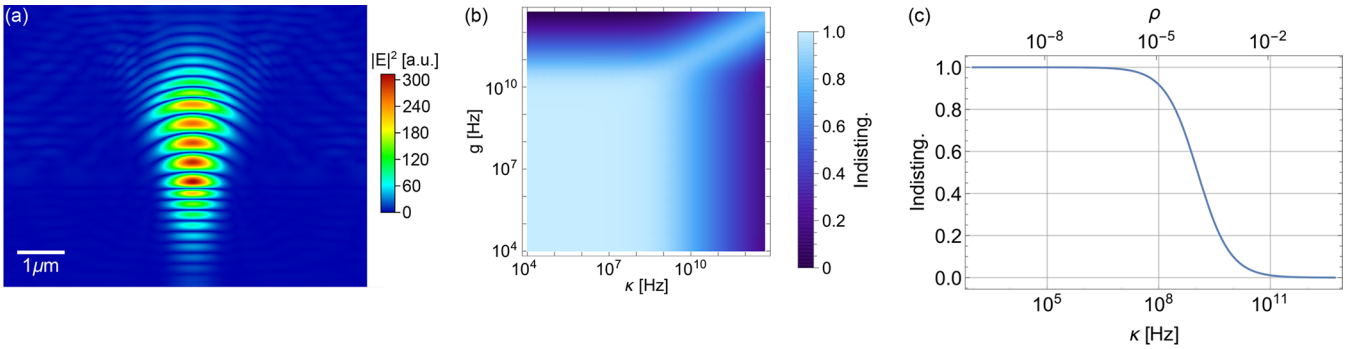

Figure 3. Theoretical modeling. (a) Electric field mode profile of a dipole emitter in the cavity obtained using FDTD simulations. (b) Indistinguishability in the weak coupling limit as a function of cavity coupling rate g and cavity line width κ. The simulations assume the photophysics of our actual emitter in the cavity. A high indistinguishability can be achieved for $g, \kappa < 10^9$ Hz. (c) Indistinguishability in the limit $g \ll 10^8$ Hz. $I > 0.9$ requires $\kappa < 124$ MHz.

photobleaching increases with decreasing wavelength[26] and due to the stopband of the cavity our excitation laser is at 450 nm. Note that the count rates at the single-photon avalanche diodes (SPADs) shown in Figure 2(e) are the raw count rates, not corrected for transmission loss or detector efficiency. The quantum emitter also emits linearly polarized light (see Figure 2(f)) with a degree of polarization (DOP) of 90.4%. The fit is obtained using a $\cos^2(\theta)$ function. A high polarization contrast is crucial for QKD applications which use polarization encoding. Increasing the DOP of not fully polarized light is always accompanied by loss, and so it sets an upper bound on the efficiency of the SPS.

Since the cavity length is tunable, the single-photon wavelength can also be tuned. Effectively, the tuning range is the line width of the free-space emission. The cavity is only sampling the free-space emission spectrum, however, so the actual single-photon count rate is the spectral overlap integral of optical cavity mode and emitter. This results in the emission rate decreasing with increasing cavity detuning.

SIMULATIONS

Numerical Modeling. We can use FDTD simulations to calculate the electric field distribution of the dipole emitter in the cavity. The electric field intensity ($|E|^2$) is shown in Figure 3(a). The simulations also show that resonance does not occur at a physical mirror separation L' which is a multiple of $\lambda/2$. This is due to the finite penetration depth of the electric field into the dielectric mirror stacks, leading to an effective cavity length. The penetration depth ξ thereby is given by

$$\xi = \frac{q\lambda/2 - L'}{2} \tag{4}$$

The physical mirror separation L' is determined by maximizing the intracavity electric field (see Supporting Information S5). Our simulations yield ξ = 122 nm. When designing the thickness of the PDMS spacer, this has to be taken into account. To reduce the computational time we simulated the longitudinal mode q = 5 instead of the experimentally realized q = 8. Nevertheless, the parameter ξ is not affected by this beyond the numerical precision of the simulation.

Applications in Quantum Technologies. We now turn to an evaluation of the SPS for two of the most common quantum information applications: quantum key distribution and quantum computing. In principle, the photon quality is sufficient for quantum key distribution, outperforming state-of-the-art protocols based on weak coherent pulses with decoy states on short and medium distances (see Supporting Information S6). On long distances decoy state protocols become more efficient. However, when evaluating the performance, it is important to keep in mind that QKD requires single-photon generation on-demand (e.g., through pulsed excitation), which has not been demonstrated yet with the current device. Moreover, since the photophysics of different emitters vary, it is not clear how well quantum emitters in hBN can be scaled. More statistics of cavity-coupled emitters are required to explore the potential of employment in quantum networks.

Notably, QKD only requires maximal entropy on all degrees of freedom which are not used for qubit encoding. Other quantum information protocols, however, do require truly indistinguishable single-photons. An example are entangling gates for single-photons for use in one-way quantum computing.[51] A measure of how indistinguishable consecutively emitted single-photons are is the interference contrast I in a Hong-Ou-Mandel experiment.[52] Unfortunately, as our cavity is pumped continuously, we cannot directly measure I. Nevertheless, we can at least theoretically calculate the expected indistinguishability. The indistinguishability of a quantum emitter with pure dephasing is given by

$$I = \frac{\gamma}{\gamma + \gamma^*} \tag{5}$$

where γ is the emission rate and γ^* is the pure dephasing rate. At room temperature we find $I = 2 \times 10^{-4}$, meaning only 1 in 5000 photons would interfere in a Hong-Ou-Mandel experiment. Even such a strongly dephasing emitter, however, can reach a regime of high indistinguishability, when coupled with a high-Q cavity. In the limit of weak coupling I modifies to

$$I = \frac{\gamma + \kappa R/(\kappa + R)}{\gamma + \kappa + 2R} \tag{6}$$

where the parameter $R = \frac{4g^2}{\kappa + \gamma + \gamma^*}$ is the effective transfer rate between the emitter and the cavity, κ is the cavity line width and g is the cavity coupling strength.[53] For our cavity parameters we find $I = 5.3 \times 10^{-3}$. While this is an improvement by a factor of 26, it is still far beyond being useful for fault-tolerant quantum computing. The indistinguishability for generalized cavity line width and coupling strength is shown in Figure 3(b). Note that in the limit of

DOI: 10.1021/acsphotonics.9b00314
ACS Photonics XXXX, XXX, XXX−XXX

strong coupling it is also possible to achieve a high indistinguishability. With the coupling strength typically $\ll 1$ GHz, a narrow cavity line width is required to maximize I. Figure 3(c) shows that $I > 90\%$ requires a cavity line width less than 124 MHz. At a reflectivity of 99.95%,[38] this line width limits the free spectral range (FSR) to 779 GHz. Compared with the free-space emission line width (5.41 THz) this means that the spectral profile of the cavity would be comb-shaped, with the cavity sampling the emitter spectrum at multiples of the FSR. Single-photons originating from different comb peaks are of course distinguishable, so a high indistinguishability requires filtering out only one peak (for example with another cavity). This, however, is balanced by a loss in efficiency. To overcome this, the natural line width of the emitter into free-space must be narrowed. Cryogenic cooling is one option to narrow the line width sufficiently.[54]

CONCLUSION

We have demonstrated coupling of a quantum emitter hosted by multilayer hBN to a confocal microcavity. The hemispherical geometries have been fabricated using FIB milling with sub-nm precision. The cavity mode volume is of the order of λ^3. The cavity improves the spectral purity of the emitter substantially, with the fwhm decreasing from 5.76 to 0.224 nm. Moreover, the cavity suppresses off-resonant noise, which allows us to improve its single-photon purity. The excited state lifetime of the emitter is also shortened by the Purcell effect by a factor of 2.3. The emission of the cavity is linearly polarized and stable over long timeframes, with no signs of photobleaching or blinking. The cavity also features a linearly tunable PDMS spacer between both mirrors, which allows in situ tuning of the single-photon line over the full free-space ZPL of the quantum emitter. This would allow us to fabricate multiple identical single-photon sources, by locking all to the same emission wavelength, making this approach fully scalable. Furthermore, the complete SPS is portable and fully self-contained within $10 \times 10 \times 10$ cm^3. The microcavity platform can also be easily adapted to other quantum emitters in 2D materials and offers a promising path toward scalable quantum information processing.

METHODS

FIB Milling. Borosilicate glass substrates with a size of 18×18 mm$^2 \times 160$ μm have been coated with 100 nm gold using electron-beam thermal evaporation to prevent substrate charging effects. The ion accelerating voltage in the FIB (FEI Helios 600 NanoLab) is 30 kV with currents $\leq$0.28 nA. The dose rate is encoded in the RGB color of a hemispherical pixel map. The dose rate to RGB value was carefully calibrated using AFM measurements. During the milling process we add I_2-gas, which ensures a smooth surface. Finally, the gold film is chemically etched using a custom-made potassium iodide ($KI:I_2:H_2O$ with ratio 4:1:40 by weight) solution. Surface characterizations before and after the KI-etching show no difference in radius or roughness. We also tried hydrofluoric acid to etch the hemispheres, but for the feature sizes required for the cavity we could not achieve a smooth surface.

Plasma Sputtering. We calibrated the deposition rate of the sputter coater (AJA) using variable angle spectroscopic ellipsometry (JA Woollam M-2000D), which measures film thickness and refractive index. At 565 nm we found $n_{SiO2} = 1.521$, $n_{TiO2} = 2.135$, and $n_{MgF2} = 1.390$. The deposition was done at room temperature. For the highly reflective coating we deposit alternating layers of SiO_2/TiO_2 with thickness of $\lambda/4n$ and the SiO_2 terminating the mirror. Due to the refractive index of MgF_2 being roughly in the middle between glass and air, the backsides of the substrates are coated with one-quarter wave layer of MgF_2, serving as an antireflective coating. To maximize the escape efficiency into one particular direction it is common to make one of the stacks thicker (e.g., 10:9), so the photons couple primarily into a single direction. For simplicity, we used 9:9 stacks, which thus introduces 50% loss.

Quantum Emitter Fabrication. The flat mirrors have been coated with 300 nm 950 PMMA A4. Multilayer hBN flakes have been exfoliated from bulk (HQGraphene) and transferred onto the PMMA layer by dry contact. Oxygen plasma etching (500 W for 2 min generated from a microwave field at a gas flow of 300 ccm^3/min) removes the PMMA around the flake as well as creates the quantum emitters. The PMMA below the flake is decomposed during the annealing, which also stabilizes the optical emission properties (more details have been published previously[20]).

Optical Characterization. Each flake has been scanned using a custom-built confocal micro-photoluminescence setup with a resolution of 0.5 μm and a spectrum has been recorded at each scanning position. The excitation laser with a wavelength of 522 nm is nonresonant with the optical transition energy of the defect. The laser light is blocked with a Semrock RazorEdge ultrasteep long-pass edge filter. With a laser pulse length of 300 fs at a repetition rate of 20.8 MHz, the setup also allows us to measure the excited state lifetime. The pulses are split into trigger and excitation pulses, and the photoluminescence is detected by a SPAD (Micro Photon Devices). The time correlation between trigger pulse and arrival time of the photoluminescence is given by a time-to-digital converter (PicoQuant PicoHarp 300). The photoluminescence is coupled via a grating to the SPAD, which makes the TRPL wavelength-sensitive. This allows us to measure the lifetime of the ZPL only. The second-order correlation function measurements have been performed using two SPADs in the exit ports of a beam splitter and under continuous excitation. We fit the function

$$g^{(2)}(\tau) = 1 - Ae^{-|\tau|/t_1} + Be^{-|\tau|/t_2} \tag{7}$$

with the anti- and bunching amplitudes A and B, and the decay times t_1 and t_2. The experimental data is normalized such that $g^{(2)}(\tau \to \infty) = 1$. The background corrected $g_c^{(2)}$ is given by

$$g_c^{(2)} = \frac{g^{(2)} - (1 - \rho^2)}{\rho^2} \tag{8}$$

with $\rho = \mathrm{SNR}/(\mathrm{SNR} + 1)$, where SNR is the signal-to-noise ratio. In addition to the long-pass filter, the photoluminescence for correlation function measurements is band-pass filtered around the ZPL. We utilize linear variable filters (Delta Optical Thin Film 3G LVLWP and 3G LVSWP) to tune center and bandwidth of the band-pass filtering system.

Cavity Alignment. The emitter on the mirror has been located and characterized in free-space. The hBN flake capable of hosting a defect (determined by flake thickness) was centered onto the mirror, making it easy to locate on the mirror. Nearby crystal flakes serve as markers for localizing the flake with the precharacterized defect. For aligning the crystal long working distance objectives in a custom-built microscope have been used, illuminated with a near-infrared LED where all

DOI: 10.1021/acsphotonics.9b00314
ACS Photonics XXXX, XXX, XXX−XXX

coatings are transparent. Each component, held and aligned with vacuum tweezers on a motorized 6-axis nanopositioning stage, is glued one after another. The adhesive used was UHU Plus Endfest 300, a two component epoxy glue, and was cured for 24 h at room temperature. Where required a second layer of glue was added and cured for another 24 h. Diagnostics were used to provide feedback for a good alignment, e.g., single-photon detection rate when aligning the cavity, combined with the spectrometer to check the cavity mode profile.

■ ASSOCIATED CONTENT

Supporting Information

The Supporting Information is available free of charge on the ACS Publications website at DOI: 10.1021/acsphotonics.9b00314.

(1) Hemisphere fabrication; (2) spin speed curves PDMS solution; (3) photographs of the device; (4) transverse mode spacing; (5) FDTD simulations; (6) QKD simulations (PDF)

■ AUTHOR INFORMATION

Corresponding Authors

*E-mail: tobias.vogl@uni-jena.de.

*E-mail: ping.lam@anu.edu.au.

ORCID

Tobias Vogl: 0000-0002-0993-0648

Yuerui Lu: 0000-0001-6131-3906

Present Address

§Institute of Applied Physics, Abbe Center of Photonics, Friedrich-Schiller-Universität Jena, 07745 Jena, Germany.

Notes

The authors declare no competing financial interest.

■ ACKNOWLEDGMENTS

This work was funded by the Australian Research Council (CE110001027, FL150100019, DE140100805, DP180103238). We thank the ACT Node of the Australian National Fabrication Facility for access to their nano- and microfabrication facilities. We also thank Hark Hoe Tan for access to the TRPL system. R.L. acknowledges support by an Australian Government Research Training Program (RTP) Scholarship.

■ REFERENCES

(1) O'Brien, J. L.; Furusawa, A.; Vučković, J. Photonic quantum technologies. *Nat. Photonics* **2009**, *3*, 687−695.

(2) Senellart, P.; Solomon, G.; White, A. High-performance semiconductor quantum-dot single-photon sources. *Nat. Nanotechnol.* **2017**, *12*, 1026−1039.

(3) Barros, H. G.; Stute, A.; Northup, T. E.; Russo, C.; Schmidt, P. O.; Blatt, R. Deterministic single-photon source from a single ion. *New J. Phys.* **2009**, *11*, 103004.

(4) Aharonovich, I.; Englund, D.; Toth, M. Solid-state single-photon emitters. *Nat. Photonics* **2016**, *10*, 631−641.

(5) Bock, M.; Lenhard, A.; Chunnilall, C.; Becher, C. Highly efficient heralded single-photon source for telecom wavelengths based on a PPLN waveguide. *Opt. Express* **2016**, *24*, 23992−24001.

(6) Tonndorf, P.; Schmidt, R.; Schneider, R.; Kern, J.; Buscema, M.; Steele, G. A.; Castellanos-Gomez, A.; van der Zant, H. S. J.; de Vasconcellos, S. M.; Bratschitsch, R. Single-photon emission from localized excitons in an atomically thin semiconductor. *Optica* **2015**, *2*, 347−352.

(7) Srivastava, A.; Sidler, M.; Allain, A. V.; Lembke, D. S.; Kis, A.; Imamoğlu, A. Optically active quantum dots in monolayer WSe2. *Nat. Nanotechnol.* **2015**, *10*, 491−496.

(8) Koperski, M.; Nogajewski, K.; Arora, A.; Cherkez, V.; Mallet, P.; Veuillen, J.-Y.; Marcus, J.; Kossacki, P.; Potemski, M. Single photon emitters in exfoliated WSe2 structures. *Nat. Nanotechnol.* **2015**, *10*, 503−506.

(9) He, Y.-M.; Clark, G.; Schaibley, J. R.; He, Y.; Chen, M.-C.; Wei, Y.-J.; Ding, X.; Zhang, Q.; Yao, W.; Xu, X.; Lu, C.-Y.; Pan, J.-W. Single quantum emitters in monolayer semiconductors. *Nat. Nanotechnol.* **2015**, *10*, 497−502.

(10) Chakraborty, C.; Kinnischtzke, L.; Goodfellow, K. M.; Beams, R.; Vamivakas, A. N. Voltage-controlled quantum light from an atomically thin semiconductor. *Nat. Nanotechnol.* **2015**, *10*, 507−511.

(11) Palacios-Berraquero, C.; Barbone, M.; Kara, D. M.; Chen, X.; Goykhman, I.; Yoon, D.; Ott, A. K.; Beitner, J.; Watanabe, K.; Taniguchi, T.; Ferrari, A. C.; Atatüre, M. Atomically thin quantum light-emitting diodes. *Nat. Commun.* **2016**, *7*, 12978.

(12) Branny, A.; Wang, G.; Kumar, S.; Robert, C.; Lassagne, B.; Marie, X.; Gerardot, B. D.; Urbaszek, B. Discrete quantum dot like emitters in monolayer MoSe2: Spatial mapping, magneto-optics, and charge tuning. *Appl. Phys. Lett.* **2016**, *108*, 142101.

(13) Klein, J.; Lorke, M.; Florian, M.; Sigger, F.; Wierzbowski, J.; Cerne, J.; Müller, K.; Taniguchi, T.; Watanabe, K.; Wurstbauer, U.; Kaniber, M.; Knap, M.; Schmidt, R.; Finley, J. J.; Holleitner, A. W. Atomistic defect states as quantum emitters in monolayer MoS_2. 2019, arXiv:1901.01042.

(14) Tran, T. T.; Bray, K.; Ford, M. J.; Toth, M.; Aharonovich, I. Quantum emission from hexagonal boron nitride monolayers. *Nat. Nanotechnol.* **2016**, *11*, 37−41.

(15) Tran, T. T.; Elbadawi, C.; Totonjian, D.; Lobo, C. J.; Grosso, G.; Moon, H.; Englund, D. R.; Ford, M. J.; Aharonovich, I.; Toth, M. Robust Multicolor Single Photon Emission from Point Defects in Hexagonal Boron Nitride. *ACS Nano* **2016**, *10*, 7331−7338.

(16) Tran, T. T.; Zachreson, C.; Berhane, A. M.; Bray, K.; Sandstrom, R. G.; Li, L. H.; Taniguchi, T.; Watanabe, K.; Aharonovich, I.; Toth, M. Quantum Emission from Defects in Single-Crystalline Hexagonal Boron Nitride. *Phys. Rev. Appl.* **2016**, *5*, 034005.

(17) Cassabois, G.; Valvin, P.; Gil, B. Hexagonal boron nitride is an indirect bandgap semiconductor. *Nat. Photonics* **2016**, *10*, 262−266.

(18) Schell, A. W.; Takashima, H.; Tran, T. T.; Aharonovich, I.; Takeuchi, S. Coupling Quantum Emitters in 2D Materials with Tapered Fibers. *ACS Photonics* **2017**, *4*, 761−767.

(19) Vogl, T.; Lu, Y.; Lam, P. K. Room temperature single photon source using fiber-integrated hexagonal boron nitride. *J. Phys. D: Appl. Phys.* **2017**, *50*, 295101.

(20) Vogl, T.; Campbell, G.; Buchler, B. C.; Lu, Y.; Lam, P. K. Fabrication and Deterministic Transfer of High-Quality Quantum Emitters in Hexagonal Boron Nitride. *ACS Photonics* **2018**, *5*, 2305−2312.

(21) Kianinia, M.; Regan, B.; Tawfik, S. A.; Tran, T. T.; Ford, M. J.; Aharonovich, I.; Toth, M. Robust Solid-State Quantum System Operating at 800 K. *ACS Photonics* **2017**, *4*, 768−773.

(22) Vogl, T.; Sripathy, K.; Sharma, A.; Reddy, P.; Sullivan, J.; Machacek, J. R.; Zhang, L.; Karouta, F.; Buchler, B. C.; Doherty, M. W.; Lu, Y.; Lam, P. K. Radiation tolerance of two-dimensional material-based devices for space applications. *Nat. Commun.* **2019**, *10*, 1202.

(23) Tawfik, S. A.; Ali, S.; Fronzi, M.; Kianinia, M.; Tran, T. T.; Stampfl, C.; Aharonovich, I.; Toth, M.; Ford, M. J. First-principles investigation of quantum emission from hBN defects. *Nanoscale* **2017**, *9*, 13575−13582.

(24) Abdi, M.; Chou, J.-P.; Gali, A.; Plenio, M. B. Color Centers in Hexagonal Boron Nitride Monolayers: A Group Theory and Ab Initio Analysis. *ACS Photonics* **2018**, *5*, 1967−1976.

(25) Bourrellier, R.; Meuret, S.; Tararan, A.; Stéphan, O.; Kociak, M.; Tizei, L. H. G.; Zobelli, A. Bright UV Single Photon Emission at Point Defects in h-BN. *Nano Lett.* **2016**, *16*, 4317−4321.

DOI: 10.1021/acsphotonics.9b00314
ACS Photonics XXXX, XXX, XXX−XXX

(26) Shotan, Z.; Jayakumar, H.; Considine, C. R.; Mackoit, M.; Fedder, H.; Wrachtrup, J.; Alkauskas, A.; Doherty, M. W.; Menon, V. M.; Meriles, C. A. Photoinduced Modification of Single-Photon Emitters in Hexagonal Boron Nitride. *ACS Photonics* **2016**, *3*, 2490−2496.
(27) Chejanovsky, N.; Rezai, M.; Paolucci, F.; Kim, Y.; Rendler, T.; Rouabeh, W.; Fávaro de Oliveira, F.; Herlinger, P.; Denisenko, A.; Yang, S.; Gerhardt, I.; Finkler, A.; Smet, J. H.; Wrachtrup, J. Structural Attributes and Photodynamics of Visible Spectrum Quantum Emitters in Hexagonal Boron Nitride. *Nano Lett.* **2016**, *16*, 7037−7045.
(28) Xu, Z.-Q.; et al. Single photon emission from plasma treated 2D hexagonal boron nitride. *Nanoscale* **2018**, *10*, 7957−7965.
(29) Choi, S.; Tran, T. T.; Elbadawi, C.; Lobo, C.; Wang, X.; Juodkazis, S.; Seniutinas, G.; Toth, M.; Aharonovich, I. Engineering and Localization of Quantum Emitters in Large Hexagonal Boron Nitride Layers. *ACS Appl. Mater. Interfaces* **2016**, *8*, 29642−29648.
(30) Ngoc My Duong, H.; Nguyen, M. A. P.; Kianinia, M.; Ohshima, T.; Abe, H.; Watanabe, K.; Taniguchi, T.; Edgar, J. H.; Aharonovich, I.; Toth, M. Effects of High-Energy Electron Irradiation on Quantum Emitters in Hexagonal Boron Nitride. *ACS Appl. Mater. Interfaces* **2018**, *10*, 24886−24891.
(31) Proscia, N. V.; Shotan, Z.; Jayakumar, H.; Reddy, P.; Cohen, C.; Dollar, M.; Alkauskas, A.; Doherty, M.; Meriles, C. A.; Menon, V. M. Near-deterministic activation of room-temperature quantum emitters in hexagonal boron nitride. *Optica* **2018**, *5*, 1128−1134.
(32) Gisin, N.; Ribordy, G.; Tittel, W.; Zbinden, H. Quantum cryptography. *Rev. Mod. Phys.* **2002**, *74*, 145−195.
(33) Kok, P.; Munro, W. J.; Nemoto, K.; Ralph, T. C.; Dowling, J. P.; Milburn, G. J. Linear optical quantum computing with photonic qubits. *Rev. Mod. Phys.* **2007**, *79*, 135−174.
(34) Vahala, K. J. Optical microcavities. *Nature* **2003**, *424*, 839−846.
(35) Kaupp, H.; Deutsch, C.; Chang, H.-C.; Reichel, J.; Hänsch, T. W.; Hunger, D. Scaling laws of the cavity enhancement for nitrogen-vacancy centers in diamond. *Phys. Rev. A: At., Mol., Opt. Phys.* **2013**, *88*, 053812.
(36) Iff, O.; Lundt, N.; Betzold, S.; Tripathi, L. N.; Emmerling, M.; Tongay, S.; Lee, Y. J.; Kwon, S.-H.; Höfling, S.; Schneider, C. Deterministic coupling of quantum emitters in WSe2 monolayers to plasmonic nanocavities. *Opt. Express* **2018**, *26*, 25944−25951.
(37) Luo, Y.; Shepard, G. D.; Ardelean, J. V.; Rhodes, D. A.; Kim, B.; Barmak, K.; Hone, J. C.; Strauf, S. Deterministic coupling of site-controlled quantum emitters in monolayer WSe2 to plasmonic nanocavities. *Nat. Nanotechnol.* **2018**, *13*, 1137−1142.
(38) Flatten, L. C.; Weng, L.; Branny, A.; Johnson, S.; Dolan, P. R.; Trichet, A. A. P.; Gerardot, B. D.; Smith, J. M. Microcavity enhanced single photon emission from two-dimensional WSe2. *Appl. Phys. Lett.* **2018**, *112*, 191105.
(39) Tran, T. T.; Wang, D.; Xu, Z.-Q.; Yang, A.; Toth, M.; Odom, T. W.; Aharonovich, I. Deterministic Coupling of Quantum Emitters in 2D Materials to Plasmonic Nanocavity Arrays. *Nano Lett.* **2017**, *17*, 2634−2639.
(40) Kim, S.; Fröch, J. E.; Christian, J.; Straw, M.; Bishop, J.; Totonjian, D.; Watanabe, K.; Taniguchi, T.; Toth, M.; Aharonovich, I. Photonic crystal cavities from hexagonal boron nitride. *Nat. Commun.* **2018**, *9*, 2623.
(41) Dolan, P. R.; Hughes, G. M.; Grazioso, F.; Patton, B. R.; Smith, J. M. Femtoliter tunable optical cavity arrays. *Opt. Lett.* **2010**, *35*, 3556−3558.
(42) Trichet, A. A. P.; Dolan, P. R.; Coles, D. M.; Hughes, G. M.; Smith, J. M. Topographic control of open-access microcavities at the nanometer scale. *Opt. Express* **2015**, *23*, 17205−17216.
(43) Liu, X.; Galfsky, T.; Sun, Z.; Xia, F.; Lin, E.-c.; Lee, Y.-H.; Kéna-Cohen, S.; Menon, V. M. Strong light-matter coupling in two-dimensional atomic crystals. *Nat. Photonics* **2015**, *9*, 30−34.
(44) Lundt, N.; Klembt, S.; Cherotchenko, E.; Betzold, S.; Iff, O.; Nalitov, A. V.; Klaas, M.; Dietrich, C. P.; Kavokin, A. V.; Höfling, S.; Schneider, C. Room-temperature Tamm-plasmon exciton-polaritons with a WSe2 monolayer. *Nat. Commun.* **2016**, *7*, 13328.
(45) Knopf, H.; Lundt, N.; Bucher, T.; Höfling, S.; Tongay, S.; Taniguchi, T.; Watanabe, K.; Staude, I.; Schulz, U.; Schneider, C.; Eilenberger, F. Integration of atomically thin layers of transition metal dichalcogenides into high-Q, monolithic Bragg-cavities: an experimental platform for the enhancement of the optical interaction in 2D-materials. *Opt. Mater. Express* **2019**, *9*, 598−610.
(46) Leifgen, M.; Schröder, T.; Gädeke, F.; Riemann, R.; Métillon, V.; Neu, E.; Hepp, C.; Arend, C.; Becher, C.; Lauritsen, K.; Benson, O. Evaluation of nitrogen- and silicon-vacancy defect centres as single photon sources in quantum key distribution. *New J. Phys.* **2014**, *16*, 023021.
(47) Hanschke, L.; Fischer, K. A.; Appel, S.; Lukin, D.; Wierzbowski, J.; Sun, S.; Trivedi, R.; Vučković, J.; Finley, J. J.; Müller, K. Quantum dot single-photon sources with ultra-low multi-photon probability. *npj Quantum Inf.* **2018**, *4*, 43.
(48) Schweickert, L.; Jöns, K. D.; Zeuner, K. D.; Covre da Silva, S. F.; Huang, H.; Lettner, T.; Reindl, M.; Zichi, J.; Trotta, R.; Rastelli, A.; Zwiller, V. On-demand generation of background-free single photons from a solid-state source. *Appl. Phys. Lett.* **2018**, *112*, 093106.
(49) Beveratos, A.; Brouri, R.; Gacoin, T.; Poizat, J.-P.; Grangier, P. Nonclassical radiation from diamond nanocrystals. *Phys. Rev. A: At., Mol., Opt. Phys.* **2001**, *64*, 061802.
(50) Pursley, B. C.; Carter, S. G.; Yakes, M. K.; Braker, A. S.; Gammon, D. Picosecond pulse shaping of single photons using quantum dots. *Nat. Commun.* **2018**, *9*, 115.
(51) Raussendorf, R.; Briegel, H. J. A One-Way Quantum Computer. *Phys. Rev. Lett.* **2001**, *86*, 5188−5191.
(52) Hong, C. K.; Ou, Z. Y.; Mandel, L. Measurement of subpicosecond time intervals between two photons by interference. *Phys. Rev. Lett.* **1987**, *59*, 2044−2046.
(53) Grange, T.; Hornecker, G.; Hunger, D.; Poizat, J.-P.; Gérard, J.-M.; Senellart, P.; Auffèves, A. Cavity-Funneled Generation of Indistinguishable Single Photons from Strongly Dissipative Quantum Emitters. *Phys. Rev. Lett.* **2015**, *114*, 193601.
(54) Dietrich, A.; Bürk, M.; Steiger, E. S.; Antoniuk, L.; Tran, T. T.; Nguyen, M.; Aharonovich, I.; Jelezko, F.; Kubanek, A. Observation of Fourier transform limited lines in hexagonal boron nitride. *Phys. Rev. B: Condens. Matter Mater. Phys.* **2018**, *98*, 081414.

DOI: 10.1021/acsphotonics.9b00314
ACS Photonics XXXX, XXX, XXX−XXX